

Entanglement Classification of Arbitrary Three-Qubit States via Artificial Neural Networks

Jorawar Singh,^{1,*} Vaishali Gulati,^{1,†} Kavita Dorai,^{1,‡} and Arvind^{1,§}

¹*Department of Physical Sciences, Indian Institute of Science Education & Research Mohali, Sector 81 SAS Nagar, Manauli PO 140306 Punjab India.*

We design and successfully implement artificial neural networks (ANNs) to detect and classify entanglement for three-qubit systems using limited state features. The overall design principle is a feed forward neural network (FFNN), with the output layer consisting of a single neuron for the detection of genuine multipartite entanglement (GME) and six neurons for the classification problem corresponding to six entanglement classes under stochastic local operations and classical communication (SLOCC). The models are trained and validated on a simulated dataset of randomly generated states. We achieve high accuracy, around 98%, for detecting GME as well as for SLOCC classification. Remarkably, we find that feeding only 7 diagonal elements of the density matrix into the ANN results in an accuracy greater than 94% for both the tasks, showcasing the strength of the method in reducing the required input data while maintaining efficient performance. Reducing the feature set makes it easier to apply ANN models for entanglement classification, particularly in resource-constrained environments, without sacrificing accuracy. The performance of the ANN models was further evaluated by introducing white noise into the data set, and the results indicate that the models are robust and are able to well tolerate noise.

I. INTRODUCTION

Entanglement, alongwith with other quantum correlations, represents a fundamental aspect of quantum mechanics that underpins the superiority of quantum information processing over classical approaches [1]. Entanglement is an essential ingredient for quantum algorithms such as Shor's algorithm and other algorithms which provide an exponential speedup over their classical counterparts [2, 3]. Furthermore, entanglement has been instrumental in enabling a range of quantum technologies, including quantum communication[4, 5], superdense coding[6], and quantum metrology[7]. Despite these advantages, the detection, estimation, and classification of quantum entanglement can be computationally formidable [8], and pose a significant challenge in the field [9].

While entanglement detection and classification are well-characterized for bipartite pure states and for general states of two-qubit systems due to the availability of positive partial transpose (PPT) criteria [10], they remain open problems for multipartite systems as well as for mixed states of larger-dimensional bipartite systems. For instance, all the mixed entangled states for two qutrits are not known, while for a 4-qubit system, the total number of distinct entanglement classes is yet to be fully delineated [11, 12]. Traditional approaches for entanglement detection utilize one-way (sufficient) conditions based on Bell inequalities, concurrence, negativity and entanglement witnesses. Oftentimes, these detection

schemes require full state tomography, which is computationally hard and requires a lot of resources [13–15].

In the present era where large scale data manipulations are possible, artificial intelligence (AI) provides innovative approaches to enhance and at times even replace, existing techniques for computation and decision making problems. AI has been successfully utilized across a wide array of fields, ranging from healthcare diagnostics [16] and climate modeling [17] to chatbots [18] and gaming [19, 20]. In the context of quantum computation and information, machine learning (ML) has been applied to several information processing tasks, including quantum error correction [21], optimization [22], quantum simulation [23], data compression [24], and verifying quantum supremacy [25].

ML-based strategies for entanglement detection include artificial neural network (ANN) models using Bell inequalities for classifying entangled states [26], deep ANN for identifying entanglement [27, 28], and validating the entanglement class of three-qubit pure states via ANN models [29]. ML has also been used to parameterize quantum states as neural networks [30, 31], to optimize measurement sets for entangled states [32], and to generate entanglement witnesses using support vector machines [33, 34], and using generative adversarial networks [35].

SLOCC (Stochastic Local Operations and Classical Communication) classification is a framework used to categorize quantum states based on their equivalence under local operations combined with classical communication. Two states $|\psi\rangle$ and $|\phi\rangle$ are considered equivalent under SLOCC if there is a non-zero probability of successfully converting $|\psi\rangle$ into $|\phi\rangle$, as well as converting $|\phi\rangle$ back into $|\psi\rangle$ under LOCC [36]. For the three-qubit system that we study in this paper, the general form of pure states upto LOCC can be written in a convenient canonical form, from which arbitrary states can be generated

* ph19023@iisermohali.ac.in

† vaishali@iisermohali.ac.in

‡ kavita@iisermohali.ac.in

§ arvind@iisermohali.ac.in

by the application of local unitaries [37]:

$$|\psi\rangle = \lambda_0|000\rangle + \lambda_1 e^{i\varphi}|100\rangle + \lambda_2|101\rangle + \lambda_3|110\rangle + \lambda_4|111\rangle$$

$$\sum_{i=0}^{i=4} |\lambda_i|^2 = 1, \quad \lambda_i \in \mathbb{R}, \quad \lambda_i \geq 0, \quad 0 \leq \varphi \leq \pi. \quad (1)$$

In a three-qubit system, there are six inequivalent SLOCC classes: Fully separable, where all qubits are separable; three biseparable classes (BS1, BS2, BS3), where specific pairs of qubits are entangled while the remaining qubit is not entangled with them; and two genuine multipartite classes, the GHZ and W classes, with each class representing different forms of maximal entanglement [38].

In this study, ANN models were designed and implemented with two main objectives: **(1.)** To detect the presence of genuine multipartite entanglement (GME) in pure three-qubit states, and **(2.)** to classify entanglement in these systems by distinguishing between six SLOCC classes, namely: fully separable (SEP), three types of biseparable states (BS1, BS2, BS3), and maximally entangled W and GHZ states. We employ different ANN models for each task. The first ANN model utilizes all 35 relevant density matrix elements, while the second model is restricted to the 7 diagonal elements. The models were trained and tested using numerically generated arbitrary pure quantum states. Our results demonstrate that even with a reduced set of features, specifically the diagonal elements alone, the ANN model can still effectively classify complex quantum states, highlighting the robustness and efficiency of this approach. It is worth noting that the high efficiency of detection of GME and classification of entanglement from only the 7 diagonal elements of the density matrix is rather surprising and points to certain hidden patterns in the data which the ANN model is able to recognize.

The rest of this paper is structured as follows: Section II covers the fundamental concepts necessary for designing our ANN models, including dataset generation II A, feature selection II B, and basics of the ANN architecture and evaluation II C. Section III contains details of our models and presents the results obtained from the GME III B and SLOCC III C models. Section IV contains a few conclusions and future directions.

II. ESSENTIALS OF ANN MODEL BUILDING

A. Dataset Generation and Data encoding

Random quantum states of the three-qubit system required to train our ANN model are generated by utilizing the qutip package [39]. The dataset ought to encompass various SLOCC classes, each corresponding to different types of entanglement in three-qubit systems, as detailed below.

Separable States: These are generated by taking the tensor product of three independent single-qubit states.

These states are unentangled across all qubits and provide examples of fully separable quantum states in our training data.

Biseparable States: These states are partially entangled, with only two of the three qubits entangled. We further categorize them into three subsets based on which qubits are entangled:

Biseparable 1 (BS1): States in this set are generated as a tensor product of a 2-dimensional ket with a 4-dimensional ket ($2 \otimes 4$), representing entanglement between the second and third qubits.

Biseparable 3 (BS3): Here, we generate states as $4 \otimes 2$ kets, where the first two qubits are entangled.

Biseparable 2 (BS2): For this set, we start by creating $4 \otimes 2$ states in a ACB qubit order, then apply a swap operation between qubits B and C to re-order qubits to the standard ABC configuration, where qubits A and C are entangled.

GHZ States: GHZ states are maximally entangled across all three qubits, where no two qubits are individually entangled. These states are represented by random kets of dimension 8.

W States: Although W states are also maximally entangled across all three qubits and belong to the 8-dimensional Hilbert space, they form a set of measure zero [40], meaning random sampling of 8-dimensional kets will not produce W states. To ensure the representation of this set, we start with the standard W state and apply local unitary transformations, which maintain W-state entanglement properties while generating variations.

To ensure that the ANN model is exposed to a wide variety of state configurations, we apply local unitary transformations to the randomly generated states from each SLOCC class (separable, biseparable, and GHZ). In a three-qubit setup, there are 8 possible ways to apply local unitary transformations to a given state: $\{\mathbb{I} \otimes \mathbb{I} \otimes \mathbb{I}, U_i \otimes \mathbb{I} \otimes \mathbb{I}, \dots, U_i \otimes U_j \otimes U_k\}$, with each U generated randomly. For each SLOCC class, we generate 125,000 states using each of the 8 local unitary transformations, resulting in a total of 1,000,000 states. The base state for each transformation is generated as described earlier. This augmentation step enhances the diversity and generalizability of the dataset, providing the ANN model with a wide range of instances from each SLOCC class, thereby improving its learning performance. For both tasks-SLOCC classification and GME detection, the same 1,000,000 states are used for training.

Having generated the input-output pairs for the ANN training, we need to encode them in a way that the network understands: The 8×8 complex valued density matrix ρ is split into two 8×8 real valued matrices comprising of the real and imaginary components of ρ . These 8×8 matrices are then flattened into column vectors, resulting in $\vec{V}_{\mathbb{R}}(\rho)$ and $\vec{V}_{\mathbb{I}}(\rho)$ of size 64×1 . These vectors are further combined into a single column vector of size

128×1 : $\vec{F} = [\vec{V}_{\mathbb{R}}(\rho) \ \vec{V}_{\mathbb{I}}(\rho)]$ which becomes the input feature vector to the ANN model.

For the GME/Non-GME identification problem, the state labels are encoded as binary numbers in a single-element vector $\vec{L}(\rho)$, with 1 indicating GME and 0 indicating Non-GME. For the SLOCC classification problem, the vector $\vec{L}(\rho)$ is a six-element column vector, with each position corresponding to a SLOCC label: [SEP, BS1, BS2, BS3, W, GHZ]. Using one-hot encoding ($\vec{L}(\rho) = [L_i(\rho)]$, $L_i(\rho) \in \{0, 1\}$ and $\sum_{i=1}^6 L_i(\rho) = 1$), we represent the class labels, assigning a value of 1 or 0 at the position corresponding to the SLOCC label. This vector $[\vec{L}(\rho)]$ becomes the output for a given input \vec{F} .

B. Feature Selection

Feature selection refers to the removal of redundant and irrelevant features from the dataset, to improve the training, performance, and efficiency of the ANN model. The input data to our ANN model are elements of a density matrix, corresponding to a three-qubit quantum state. Given that the density matrix is Hermitian with a trace of 1, we discard the upper triangular part, along with one element from the principal diagonal, without any loss of information. This reduces the matrix to 28 complex elements and 7 real elements, which translates into 63 real numbers used as input features for the ANN. We further apply univariate selection over these remaining 63 features to assign importance scores to each of the features.

Univariate selection is a feature selection method that evaluates the relationship between an individual feature and the target variable, and applies statistical tests to estimate the importance of each feature for the classification task at hand. We use the ANOVA (Analysis of Variance) F-test to assign importance scores to our features [41–43]. The ANOVA F-test partitions the dataset according to class labels and computes the mean value of each feature within these groups. It then compares two sources of variability: between-group variance (the extent to which the mean values differ across the groups) and within-group variance (the variability of feature values within each group). A feature is considered significant if the between-group variance is substantially larger than the within-group variance, indicating that the feature effectively distinguishes between classes.

C. Model Construction and Evaluation

A basic feed-forward neural network (FFNN) consists of three main components: an input layer, responsible for loading the features; one or more hidden layers, where the network learns relationships through the adjustment of weights and biases; and an output layer, which predicts the labels corresponding to the input. Each layer applies

an activation function (such as ReLU or sigmoid) which introduces non-linearity to the network, enabling it to model complex patterns in the data [44].

To train the FFNN, we split the dataset into a 80% training set and 20% validation set. While the model uses states in the training set to learn the patterns in the data, the validation set states are used to observe the learning process and ensure that the model does not overfit the data. The FFNN is trained using a process called backpropagation, which adjusts the model’s weights and biases to improve performance. Backpropagation operates by calculating a loss function (or cost function) that measures the error between the predicted and true labels for the training dataset. This loss is minimized by iteratively updating the weights of the network over a series of passes through the training data, known as epochs [44]. As training progresses, the model refines its predictions by learning from errors, aiming to reduce the overall loss.

The training process is monitored by observing the trends in the values of the indicators: training loss, training accuracy, validation loss, and validation accuracy with respect to the epochs (total training time). These indicators are used to tune hyperparameters such as the number of neurons, number of hidden layers, learning rate, number of epochs, and batch size. The values of these indicators reflect the optimization process, which is performed using the stochastic gradient descent technique called “Adam” with a fixed learning rate [45]. The goal of the optimization is to minimize the loss values over the training set. While a proper training of the model is reflected by a simultaneous decrease in training and validation loss, overfitting typically manifests as increasing validation loss coupled with decreasing training loss, signaling that the model is learning the specific details of the training data (including noise) rather than general patterns. Overfitting can generally be avoided by not using too complex a model and limiting the number of epochs.

The performance of a trained model is commonly assessed using the accuracy metric (A). Accuracy measures how well the model’s predictions align with the true labels by calculating the ratio of correct predictions to the total number of predictions made. It is expressed as:

$$A = \frac{\sum \text{Correct predictions per class}}{\text{Total predictions}} \quad (2)$$

In this equation, the numerator sums the number of correct predictions for each class, and the denominator represents the total number of predictions, including both correct and incorrect ones.

Figure 1 presents an overview of the data processing pipeline and the structure of the ANN models. As described in previous subsections, feature selection is applied to eliminate redundant features from the input density matrix, ρ , and to rank the remaining features in descending order of their importance, which is assessed using univariate selection via the ANOVA F-test. This process ensures that only relevant features are retained,

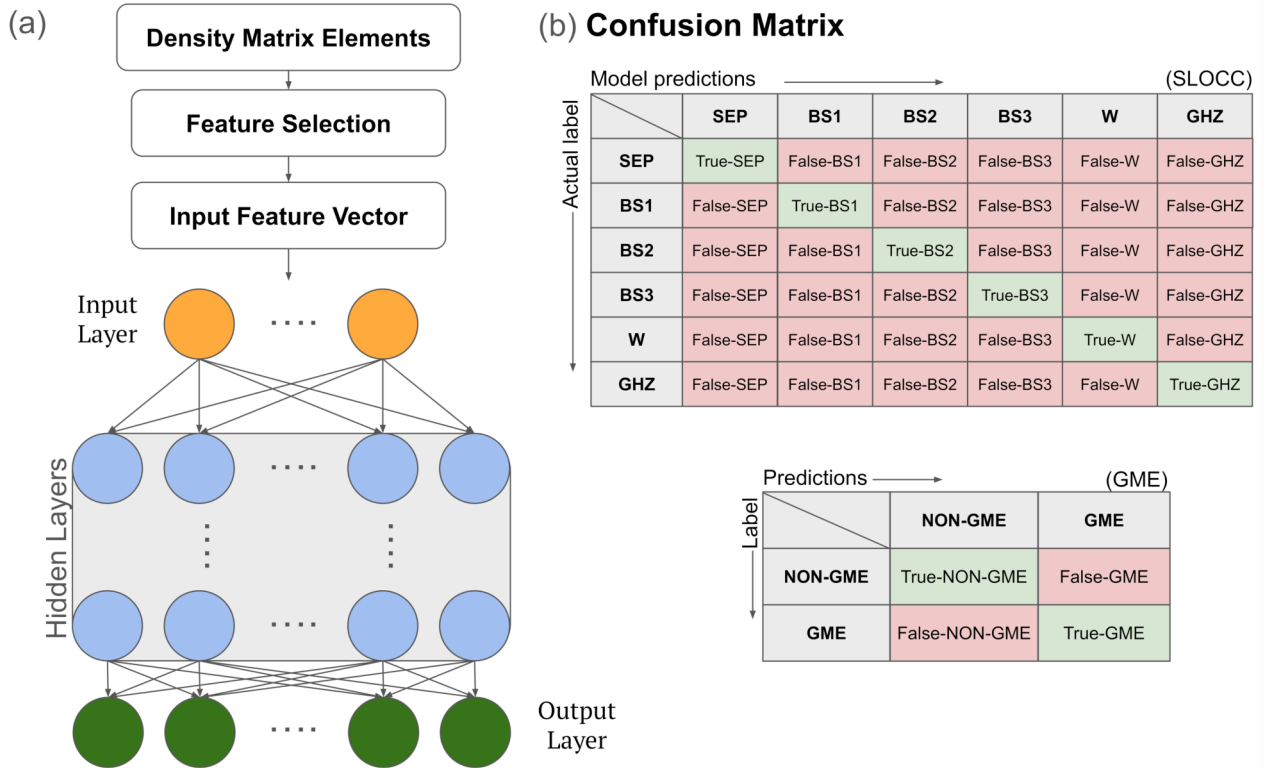


FIG. 1. (Color online) The schematic of the ANN-based entanglement classification protocol is shown in panel (a). For both GME and SLOCC tasks, the raw complex density matrix data is first simplified to real numbers, followed by feature selection to remove redundant and irrelevant features. The selected features, based on univariate selection, are then fed into the respective GME and SLOCC ANN models. The input layer for the models is shown in orange, the hidden layers are in blue, and the output layer is in green. Panel (b) depicts the confusion matrices for the two models, which can be used to access the overall performance of the model as well as its effectiveness for each individual target class.

reducing the dimensionality of the input space and simplifying the removal of irrelevant features, if any. The selected features are subsequently fed into the ANN model to perform the classification task.

Figure 1(a) illustrates the general ANN architecture for the entanglement classification problem. The architecture consists of an input layer with N neurons, where N corresponds to the number of features extracted from the density matrix, followed by a series of hidden layers with a varying number of neurons, and finally the output layer with number of neurons depending upon the classification problem. There are 6 neurons in the output layer for SLOCC classification and 1 in case of GME detection.

The number of hidden layers and neurons in the hidden layers is initially set using a heuristic, where, the number of neurons in the i -th hidden layer, N^i , is set to approximately half of the number of neurons in the previous layer, N^{i-1} , following the formula:

$$N^i = \frac{(N^{i-1} + N^{i-1} \bmod 2)}{2}$$

where $N^0 (= N)$ represents the number of neurons in the input layer. This configuration is then fine-tuned based on the complexity of the problem, as outlined in [46].

The heuristic aims to gradually reduce the number of neurons in deeper layers, balancing the complexity of the model while preventing overfitting. The formula halves the number of neurons with a small adjustment for even or odd numbers (due to the mod operation). This setup provides a reasonable starting point, which is later refined through trial and error depending on the specific problem.

The model classifies input density matrices, ρ , as either exhibiting or not exhibiting GME, with the final output layer consisting of a single neuron that outputs a probability, $0 \leq p \leq 1$. This probability indicates the likelihood that the input state belongs to the GME class. A probability value closer to 1 suggests the state has GME, while a value closer to 0 indicates that it does not.

For the SLOCC entanglement classification problem, the general architecture remains the same, with input layer of N neurons, followed by a series of hidden layers. The output layer for this task consists of 6 neurons, each representing one of the six SLOCC entanglement classes: SEP, BS1, BS2, BS3, W, and GHZ. The output of the ANN is a probability distribution $p_1, p_2, p_3, p_4, p_5, p_6$, where each p_i denotes the probability that the input state belongs to class i . The class with the

highest probability is selected as the predicted label. For instance, if p_4 is the largest, the input state is classified as belonging to the BS3 class. In both models, the predicted label is then compared to the true class label of the state. If the predicted label matches the true label, the state is considered correctly classified, and the accuracy for that state is recorded as 1. If the predicted label differs from the true label, the state is misclassified, and the accuracy is 0.

This classification performance, including the errors, of the model for each output class is visualized using a confusion matrix, as shown in Figure 1(b), which compares the predicted and true labels of the states classified by the ANN. Each entry in the matrix represents the number of states for which the predicted class label (assigned by the ANN) matches or differs from the true class label. The confusion matrix also allows an easy calculation of the accuracy A of the model - by summing the main diagonal entries and dividing it by the total number of entries [44, 47]. The smaller table in Figure 1(b) shows the confusion matrix for GME classification. Misclassifications are categorized as ‘False Non-GME’—instances where GME cases were incorrectly predicted as non-GME—and ‘False GME’—cases where non-GME instances were mistakenly classified as GME. For the SLOCC case, (SLOCC Table in Figure 1(b)), a correctly classified state is indicated by entries like "True-SEP", meaning the true label and the predicted label are both SEP (separable). Similarly, "True-BS1", "True-BS2", etc., represent correct classifications for other SLOCC classes. Misclassified states are denoted by entries such as "False-SEP", indicating that a state with a true label other than SEP state was misclassified as SEP by the ANN. For each SLOCC entanglement class, the confusion matrix tracks both correctly and incorrectly predicted labels. This allows us to evaluate the performance of the ANN across all classes and identify which entanglement categories are more prone to classification errors.

III. RESULTS AND DISCUSSION

A. Reduction of Selected Features

To address the classification problem, we numerically generated a dataset of 6,000,000 quantum states, with each class represented by 1,000,000 states. To evaluate the relative importance of each feature for classification, we employed the “f classif” function along with the “Select K Best” method from the Sklearn library [48]. These methods calculate ANOVA F-values, which provide scores indicating each feature’s significance in the classification task. Table III presents a sample of the top-ranking features and their corresponding ANOVA F-values from one specific run, out of many performed. After performing multiple runs with different datasets, we observed a consistent pattern: the

Feature No.	Feature	SLOCC	GME
1	$\mathbf{Re}(\rho_{22})$	20275.73	39573.50
2	$\mathbf{Re}(\rho_{44})$	20192.56	39899.69
3	$\mathbf{Re}(\rho_{11})$	20120.34	39422.10
4	$\mathbf{Re}(\rho_{55})$	6768.37	13527.75
5	$\mathbf{Re}(\rho_{66})$	6724.48	13335.46
6	$\mathbf{Re}(\rho_{33})$	6687.62	13151.14
7	$\mathbf{Re}(\rho_{00})$	2288.79	4650.39
8	$\mathbf{Im}(\rho_{07})$	2.75	0.13
9	$\mathbf{Re}(\rho_{23})$	2.45	0.06
10	$\mathbf{Im}(\rho_{24})$	2.14	1.73

TABLE I. ANOVA F-values (Feature Scores) for top 10 features for the SLOCC and GME ANN models.

top 7 features always emerged from the specific density matrix elements— $\mathbf{Re}(\rho_{00})$, $\mathbf{Re}(\rho_{11})$, $\mathbf{Re}(\rho_{22})$, $\mathbf{Re}(\rho_{33})$, $\mathbf{Re}(\rho_{44})$, $\mathbf{Re}(\rho_{55})$, and $\mathbf{Re}(\rho_{66})$. While the ranking of these features varied slightly between runs, these 7 features consistently occupied the top positions. Additionally, there was a marked drop in the ANOVA F-values after the 7th feature, indicating a significant difference in importance between these top features and the remaining 56. We then evaluate whether an ANN model using only these top 7 features can achieve performance comparable to a model that uses all 63 features for both classification problems.

B. GME Classification via ANN

We use the Keras API [49] with Tensorflow backend [50] for the construction, optimization, and analysis of the ANN models. We begin by constructing an artificial neural network (ANN) model utilizing all $N = 63$ input features. After extensive hyperparameter tuning to optimize accuracy, the resulting model architecture consists of layers with the following neuron structure: $N - 64 - 32 - 16 - 8 - 4 - O$, where the output layer has a single neuron ($O = 1$). Each hidden layer employs the ReLU activation function ($ReLU(x) = \max(0, x)$), while the output layer uses the sigmoid activation function, defined as:

$$\sigma(x) = \frac{1}{1 + e^{-x}} \quad (3)$$

In this equation, x represents the weighted average of the inputs passed from the final hidden layer, and $\sigma(x)$ outputs the probability that the given input belongs to the target class. This choice of activation function in the output layer is standard for binary classification tasks, where the output is interpreted as a probability.

The model’s loss function is binary cross-entropy, which is commonly used for binary classification problems. It quantifies the difference between the predicted probabilities and the actual class labels. The binary

cross-entropy loss is given by:

$$\text{Loss} = -\frac{1}{N} \sum_{i=1}^N [y_i \ln(p_i) + (1 - y_i) \ln(1 - p_i)] \quad (4)$$

where N is the total number of data points (or states), $y_i = L_i(\rho)$ is the actual class label for the i -th data point, and p_i is the predicted probability of that point belonging to the target class, i.e. $\sigma(x)$.

The model is trained using the Adam optimizer, with a learning rate of 0.0025 and a batch size of 5000. Training is conducted over 100 epochs, leading to an average accuracy of 0.998 ± 0.001 on the test set, indicating highly effective classification performance.

Based on the results from univariate feature selection with ANOVA, we assessed the model's performance using only the top 7 features, specifically the diagonal elements of the density matrix. Using these 7 features with the original model architecture and hyperparameters, we observed a decrease in accuracy of approximately 2%. However, after fine-tuning the model to better accommodate the reduced input dimension (now structured as $N - 64 - 32 - 16 - O$) and extending the training duration to 200 epochs, the accuracy loss was nearly eliminated. This resulted in an average test set accuracy of 0.992 ± 0.002 , indicating that the model performs well even with a reduced set of input features.

The ANN architecture for the GME classification problem is illustrated in Scheme A and Scheme B, which correspond to models using 63 features and 7 features, respectively, as shown in Figure 2. In these diagrams, orange circles represent the input layer, while the hidden layers are depicted in blue, and the output layer is shown in green. Each layer is labeled with its activation function and the number of neurons it contains, which are specified in brackets.

Table II presents the average performance of ANN models in classifying data into Non-GME and GME categories, using two different feature sets: 63 features and 7 features. The models demonstrate high classification accuracy across both categories. For Non-GME data, the model achieves an accuracy of 0.98 with 63 features and 0.99 with 7 features. For GME data, the model attains an accuracy of 0.99 with 63 features and 0.98 with 7 features. The overall average accuracy for the models is 0.99, regardless of whether 63 or 7 features are used. This indicates that the ANN models perform consistently well in distinguishing between Non-GME and GME states, even when using a reduced number of features.

C. SLOCC Classification via ANN

Similar to the GME classification case, we start with an ANN model that uses 63 input features. The architecture of the hidden layers is the same as before, comprising a sequence of layers with $64 - 32 - 16 - 8 - 4$ neurons, each using the ReLU activation function. The output layer

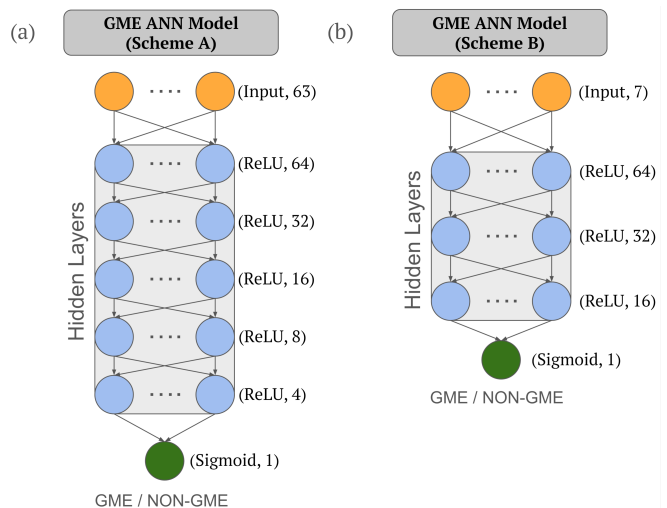


FIG. 2. GME Classification ANN Schemes: Scheme A (shown in panel (a)) utilizes 63 input features, while Scheme B (shown in panel (b)) uses 7 input features. Both schemes predict the probability of the input state having genuine multipartite entanglement (GME) or not. The input layer is represented with orange circles, the hidden layers with blue, and the output layer with green.

Class	SLOCC			Class	GME	
	63 F	7 F	7 F (Hier.)		63 F	7 F
FS	0.96	0.91	0.93	Non GME	0.98	0.99
BS1	0.98	0.95	0.97			
BS2	0.98	0.96	0.96			
BS3	0.98	0.96	0.96			
W	0.97	0.84	0.91	GME	0.99	0.98
GHZ	0.97	0.86	0.93			
Average	0.98	0.91	0.94		0.99	0.99

TABLE II. Average performance of SLOCC and GME ANN models across respective classification classes. "63F" and "7F" represent models that use 63 and 7 features, respectively. "7F (hier.)" refers to the hierarchical 3-model SLOCC ANN setup, highlighting the difference in model performance with and without the hierarchical structure.

consists of 6 neurons and utilizes the softmax activation function, defined as:

$$\sigma(x_i) = \frac{e^{x_i}}{\sum_{j=1}^C e^{x_j}}, \quad \text{for } i = 1, 2, \dots, C \quad (5)$$

Again, x_i represents the weighted average of the inputs from the final hidden layer and $\sigma(x_i)$ represents the probability of the state belonging to the i -th class, with C denoting the total number of classes.

Following the standard choice, we use "categorical cross-entropy" as the loss function, defined as:

$$\text{Loss} = -\frac{1}{N} \sum_{j=1}^N \left(\sum_{i=1}^C y_i^j \ln(p_i^j) \right) \quad (6)$$

where N is the total number of data points, C is the total number of classes, $y_i^j = L_i^j(\rho)$ and $p_i^j = \sigma(x_i)$ are the true class label and predicted probability for the j -th data point in the i -th class respectively.

The model is trained for 1000 epochs using the Adam optimizer with a learning rate of 0.0025 and a batch size of 5000, resulting in an average test set accuracy of 0.984 ± 0.002 .

For the SLOCC classification model using only 7 features, the overall accuracy decreased to approximately 86%. Despite improvements up to 91% with further hyperparameter tuning, the model's performance for the W and GHZ classes remained around 85%. The detailed accuracy for each SLOCC class along with the average accuracy of the model is tabulated in Table II.

To address this issue, we introduced a hierarchical multi-ANN structure and trained three distinct models:

1. **FS-NOT**: This model has an architecture of $N - 32r - 32r - 16l - 16l - 16l - O$, where r and l denote ReLU and linear activations, respectively, and $O = 2$. It classifies inputs as either separable or not separable.
2. **BS-GME**: This model follows the structure $N - 32r - 16r - 8r - 4l - O$, with $O = 4$. It classifies inputs into one of the biseparable classes (BS1, BS2, BS3) or as GME, which encompasses the W and GHZ classes.
3. **GHZ-W**: This model features an architecture of $N - 128r - 64r - 32r - 16r - 8r - 4l - O$, where $O = 2$. It differentiates between GHZ and W classes.

The input state is first processed by the FS-NOT model. If the output is classified as a separable class, the classification task is complete. However, if the output indicates a non-separable class, it is further analyzed by the BS-GME model, which classifies it into one of {BS1, BS2, BS3, GME}. The biseparable outputs from this model are considered final, while the GME states are forwarded to the GHZ-W model. The GHZ-W model then differentiates between the GHZ and W classes, completing the classification task.

With this hierarchical approach, we achieve an overall test set accuracy of 0.940 ± 0.003 . The accuracies for the GHZ and W classes are 0.932 ± 0.004 and 0.910 ± 0.006 , respectively. The performance of this approach for each class is detailed in Table II. The architecture of the SLOCC models, along with details of the hidden and output layers of the submodels, is illustrated in Figure 3. The hidden layers are depicted in blue, while the output layers are shown in green.

D. State Vectors vs Density Matrices as ANN Inputs

The analysis of the previous section clearly demonstrates that seven features dominate in determining the

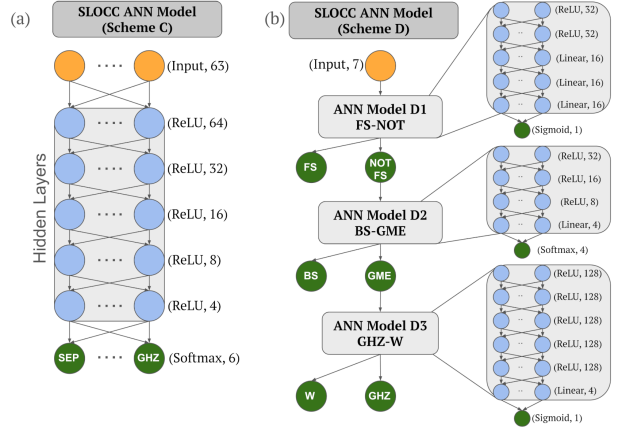


FIG. 3. SLOCC Classification ANN Schemes: Scheme C (shown in panel (a)) represents a single ANN model that takes 63 density matrix elements as input features and outputs the probability for each of the six SLOCC classes. Scheme D (shown in panel (b)) consists of a hierarchical system of three sequential ANN models to perform SLOCC classification. ANN Model D1 takes 7 diagonal density matrix elements as input and predicts whether the state belongs to the FS class. ANN Model D2 then classifies the states that are non-FS, distinguishing between GME and BS classes. Finally, ANN Model D3 further refines the classification of GME states, separating them into GHZ and W classes. Input layers are shown in orange, hidden layers in blue, and output layers in green. The internal structure of each submodel in Scheme D is displayed on the right.

presence of GME as well in establishing the entanglement class for three-qubit pure states. A natural question that arises is why did we use density matrices as inputs to the ANN model and not state vectors (represented by 15 real parameters), since it is already intuitively known that there are at most 15 features in the problem! We hence carried out the analysis to make a comparison and surprisingly, discovered that the ANN was not able to identify the seven important features when given the 15 parameter state vector as an input, and it is in fact advantageous to use density matrices.

A three-qubit pure state can be written in the computational basis with complex coefficients c_j as

$$|\psi\rangle = c_0|000\rangle + c_1|001\rangle + c_2|010\rangle + c_3|011\rangle + c_4|100\rangle + c_5|101\rangle + c_6|110\rangle + c_7|111\rangle$$

$$\text{with } \sum_{j=1}^7 |c_j| = 1. \quad (7)$$

Thus we have 15 real parameters representing this family of states. Using the ANOVA-F analysis of these 15 coefficients, we rated the features according to their importance to the classification task. The top 10 contributors are shown in Table III. As evident from the tabulated values, the difference between the scores is too low to convincingly determine a single minimal set of contributing features.

Feature No.	Feature	SLOCC	Feature	GME
1	$\text{Re}(c_7)$	2750.58	$\text{Re}(c_7)$	4388.55
2	$\text{Im}(c_0)$	1.45	$\text{Re}(c_4)$	1.90
3	$\text{Im}(c_5)$	1.42	$\text{Re}(c_2)$	1.53
4	$\text{Re}(c_0)$	1.41	$\text{Im}(c_1)$	1.40
5	$\text{Im}(c_6)$	1.27	$\text{Re}(c_1)$	1.37
6	$\text{Im}(c_2)$	1.25	$\text{Im}(c_5)$	1.07
7	$\text{Re}(c_5)$	1.24	$\text{Im}(c_6)$	1.03
8	$\text{Re}(c_3)$	1.03	$\text{Re}(c_3)$	0.93
9	$\text{Im}(c_4)$	0.95	$\text{Im}(c_4)$	0.90
10	$\text{Re}(c_6)$	0.84	$\text{Im}(c_3)$	0.77

TABLE III. ANOVA F-values (Feature Scores) for the top 10 features for the SLOCC and GME ANN models.

Following the score analysis, we trained the ANN models using all 15 features, and using the top 9 contributors, and the top 7 contributors. The drop in accuracy for the 7 feature model was very significant and hence this model is not useful. The loss in accuracy when reducing the feature set to 9 is low for GME detection, but quite significant for SLOCC classification. The hierarchical model structure for SLOCC classification is unable to circumvent this loss. Therefore, by using the state vector representation for quantum states, the minimum number of features required for an ANN model to faithfully classify states remains the same as the number of unique parameters of the quantum state. This justifies the use of density matrices in our analysis. Another reason for using density matrices is that in real-life situations, for example while working with experimental data, we may have to work with noisy (mixed) states, which will anyway require the states to be represented in terms of density matrices.

E. Noise Tolerance

In order to study the noise tolerance of our ANN model, we add white noise to the states. For a three-qubit pure quantum state ρ , we consider the noisy state ρ' where a real positive parameter $p \leq 1$ determines the amount of noise added to the state:

$$\rho' = (1 - p)\rho + p\mathbb{I} \quad (8)$$

We restrict our analysis to the regime where added noise is a few percent. The same method is used to add noise to the test dataset and to the training dataset.

We use the ANN trained on the noise-free training set to detect and classify entanglement of noise-added states and we find that the efficiency of the network decreases very rapidly, even with small amount of added noise. Table IV shows this decline for the GME as well as the SLOCC classification problem when we consider a test dataset with 0%, 1%, and 2% noise.

We next consider adding noise to the training dataset and train the network again with 2% added noise. We then use this network to detect and classify entanglement

Model	Test Set Noise					
	0%		1%		2%	
	GME	SLOCC	GME	SLOCC	GME	SLOCC
63F	1.00	0.97	0.98	0.85	0.88	0.72
7F	0.99	0.92	0.43	0.30	0.35	0.24
7F Hier	–	0.93	–	0.28	–	0.20

TABLE IV. Decline of accuracy of the ANN trained on noiseless states for detecting entanglement and for the SLOCC classification of noisy states with different noise values.

of three-qubit noisy states. The results are summarized in Table V. We evaluate the model on a test dataset with noise values 0%, 1% and 2%, respectively.

Model	Test Set Noise					
	0%		1%		2%	
	GME	SLOCC	GME	SLOCC	GME	SLOCC
63F	0.99	0.81	0.99	0.91	1.00	0.98
7F	0.62	0.26	0.70	0.32	0.99	0.92
7F Hier	–	0.30	–	0.38	–	0.90

TABLE V. Accuracy of the ANN trained on noisy states for detecting entanglement and for the SLOCC classification of noisy states with different noise values.

Clearly the network trained with added noise performs much better when detecting and classifying noisy states. There also seems to be a correlation between the amount of noise used for training and the amount of noise present in the test dataset states.

Noisy states are mixed states, and mixed quantum states for a three-qubit system constitute a much larger and more complex set. It well known that their entanglement classification is not straightforward. Our aim here was not to undertake the full fledged problem of entanglement detection and classification for mixed states, but to study the noise tolerance of our ANN models which were designed for pure states.

IV. CONCLUSIONS

We demonstrate the effectiveness of an artificial neural network (ANN) model in accurately classifying a random three-qubit pure state into one of six SLOCC inequivalent entanglement classes and detecting the presence of genuine multipartite entanglement (GME) even with partial data. We map 35 density matrix elements (7 real and 28 imaginary) from the pure quantum state of a three-qubit system to 63 ANN input features. The ANN models are trained on a dataset of 10^6 numerically generated three-qubit quantum states. Our results indicate that the ANN model achieves high accuracies (exceeding 94%) for both GME detection and SLOCC classification, using as few as 7 features. Hence, the ANN model is clearly able to identify a hidden pattern in the diagonal elements of the three-qubit states. Further, we evaluate the performance of the ANN models on noisy datasets by

introducing white noise to the test dataset. Our results demonstrate that the ANN models are robust and well tolerant towards noise.

Future directions include expanding the model to higher-dimensional systems and implementing advanced feature selection techniques and integrating hybrid machine learning models to improve classification accuracy and efficiency. Additionally, addressing the robustness of the model against noise through strategies such as data

augmentation and regularization is essential for practical applications and work is being carried out in our group on using ANN models to classify entanglement in mixed states. Exploring alternative neural network architectures for specific quantum platforms can further refine the models and align them with real-world quantum systems, ultimately paving the way for real-time classification capabilities.

-
- [1] M. A. Nielsen and I. L. Chuang, *Quantum Computation and Quantum Information* (Cambridge University Press, 2010).
- [2] P. W. Shor, in *Proceedings 35th Annual Symposium on Foundations of Computer Science* (1994) pp. 124–134.
- [3] K. Blekos, D. Brand, A. Ceschini, C.-H. Chou, R.-H. Li, K. Pandya, and A. Summer, *Phys. Rep.* **1068**, 1 (2024).
- [4] C. H. Bennett, G. Brassard, C. Crépeau, R. Jozsa, A. Peres, and W. K. Wootters, *Phys. Rev. Lett.* **70**, 1895 (1993).
- [5] A. K. Ekert, *Phys. Rev. Lett.* **67**, 661 (1991).
- [6] C. H. Bennett and S. J. Wiesner, *Phys. Rev. Lett.* **69**, 2881 (1992).
- [7] V. Giovannetti, S. Lloyd, and L. Maccone, *Science* **306**, 1330 (2004).
- [8] S. Gharibian, *Quantum Info. Comput.* **10**, 343–360 (2010).
- [9] O. Gühne and G. Tóth, *Phys. Rep.* **474**, 1 (2009).
- [10] M. Horodecki, P. Horodecki, and R. Horodecki, *Phys. Lett. A* **223**, 1 (1996).
- [11] F. Verstraete, J. Dehaene, B. De Moor, and H. Verschelde, *Phys. Rev. A* **65**, 052112 (2002).
- [12] D. Li, X. Li, H. Huang, and X. Li, *Phys. Rev. A* **76**, 052311 (2007).
- [13] J. S. Bell, *Phys. Phys. Fiz.* **1**, 195 (1964).
- [14] W. K. Wootters, *Quantum Info. Comput.* **1**, 27–44 (2001).
- [15] D.-D. Dong, L.-J. Li, X.-K. Song, L. Ye, and D. Wang, *Phys. Rev. A* **110**, 032420 (2024).
- [16] A. Esteva, A. Robicquet, B. Ramsundar, V. Kuleshov, M. DePristo, K. Chou, C. Cui, G. Corrado, S. Thrun, and J. Dean, *Nat. Med* **25**, 24 (2019).
- [17] M. Reichstein, G. Camps-Valls, B. Stevens, M. Jung, J. Denzler, N. Carvalhais, and Prabhat, *Nature* **566**, 195 (2019).
- [18] T. Brown, B. Mann, N. Ryder, M. Subbiah, J. D. Kaplan, P. Dhariwal, A. Neelakantan, P. Shyam, G. Sastry, A. Askell, S. Agarwal, A. Herbert-Voss, G. Krueger, T. Henighan, R. Child, A. Ramesh, D. Ziegler, J. Wu, C. Winter, C. Hesse, M. Chen, E. Sigler, M. Litwin, S. Gray, B. Chess, J. Clark, C. Berner, S. McCandlish, A. Radford, I. Sutskever, and D. Amodei, in *Advances in Neural Information Processing Systems*, Vol. 33, edited by H. Larochelle, M. Ranzato, R. Hadsell, M. Balcan, and H. Lin (Curran Associates, Inc., 2020) pp. 1877–1901.
- [19] J. Togelius, G. N. Yannakakis, K. O. Stanley, and C. Browne, *IEEE Trans. Comput. Intell. AI Games.* **3**, 172 (2011).
- [20] M. I. Jordan and T. M. Mitchell, *Science* **349**, 255 (2015).
- [21] S. Varsamopoulos, B. Criger, and K. Bertels, *Quantum Sci. Technol.* **3**, 015004 (2017).
- [22] M. Cerezo, A. Arrasmith, R. Babbush, S. C. Benjamin, S. Endo, K. Fujii, J. R. McClean, K. Mitarai, X. Yuan, L. Cincio, and P. J. Coles, *Nat. Rev. Phys.* **3**, 625 (2021).
- [23] I. Kassal, J. D. Whitfield, A. Perdomo-Ortiz, M.-H. Yung, and A. Aspuru-Guzik, *Annu. Rev. Phys. Chem.* **62**, 185 (2011).
- [24] S. Aaronson and D. Gottesman, *Phys. Rev. A* **70**, 052328 (2004).
- [25] A. W. Harrow and A. Montanaro, *Nature* **549**, 203 (2017).
- [26] Y.-C. Ma and M.-H. Yung, *npj Quantum Inf.* **4**, 34 (2018).
- [27] M. Krawczyk, J. Pawłowski, M. M. Maška, and K. Roszak, *Phys. Rev. A* **109**, 022405 (2024).
- [28] J. Ureña, A. Sojo, J. Bermejo-Vega, and D. Manzano, *Sci. Rep.* **14**, 18109 (2024).
- [29] V. Gulati, S. Siyanwal, Arvind, and K. Dorai, “Ann-enhanced detection of multipartite entanglement in a three-qubit nmr quantum processor,” (2024), arXiv:2409.19739 [quant-ph].
- [30] C. Harney, S. Pirandola, A. Ferraro, and M. Paternostro, *New J. Phys.* **22**, 045001 (2020).
- [31] C. Harney, M. Paternostro, and S. Pirandola, *New J. Phys.* **23**, 063033 (2021).
- [32] M. Yosefpor, M. R. Mostaan, and S. Raeisi, *Quantum Sci. Technol.* **5**, 045006 (2020).
- [33] C. Sanavio, E. Tignone, and E. Ercolessi, *Eur. Phys. J. Plus* **138**, 936 (2023).
- [34] A. C. Greenwood, L. T. Wu, E. Y. Zhu, B. T. Kirby, and L. Qian, *Phys. Rev. Appl.* **19**, 034058 (2023).
- [35] Y. Chen, Y. Pan, G. Zhang, and S. Cheng, *Quantum Sci. Technol.* **7**, 015005 (2021).
- [36] C. H. Bennett, S. Popescu, D. Rohrlich, J. A. Smolin, and A. V. Thapliyal, *Phys. Rev. A* **63**, 012307 (2000).
- [37] A. Acin, A. Andrianov, E. Jane, and R. Tarrach, *J. Phys. A Math. Theor.* **34**, 6725 (2001).
- [38] W. Dür, G. Vidal, and J. I. Cirac, *Phys. Rev. A* **62**, 062314 (2000).
- [39] J. Johansson, P. Nation, and F. Nori, *Comput. Phys. Commun.* **183**, 1760 (2012).
- [40] M. Enríquez, F. Delgado, and K. Życzkowski, *Entropy* **20** (2018), 10.3390/e20100745.
- [41] B. J. Feir-Walsh and L. E. Toothaker, *Educ. Psychol. Meas.* **34**, 789 (1974).
- [42] A. Gelman, *Ann. Stat.* **33**, 1 (2005).
- [43] E. Ostertagova and O. Ostertag, *Am. J. Mech. Eng.* **1**, 256 (2013).
- [44] J. Berner, P. Grohs, G. Kutyniok, and P. Petersen, “The

- modern mathematics of deep learning,” in *Mathematical Aspects of Deep Learning*, edited by P. Grohs and G. Kutyniok (Cambridge University Press, 2022) p. 1–111.
- [45] S. Sun, Z. Cao, H. Zhu, and J. Zhao, *IEEE Trans Cybern* **50**, 3668 (2020).
- [46] P. Gaurang, A. Ganatra, Y. Kosta, and D. Panchal, *Int. J. Comput. Theory Eng.* **3**, 332 (2011).
- [47] I. M. De Diego, A. R. Redondo, R. R. Fernández, J. Navarro, and J. M. Moguerza, *Appl Intell* **52**, 12049 (2022).
- [48] F. Pedregosa, G. Varoquaux, A. Gramfort, V. Michel, B. Thirion, O. Grisel, M. Blondel, P. Prettenhofer, R. Weiss, V. Dubourg, J. Vanderplas, A. Passos, D. Cournapeau, M. Brucher, M. Perrot, and Édouard Duchesnay, *J. Mach. Learn. Res.* **12**, 2825 (2011).
- [49] F. Chollet *et al.*, “Keras,” <https://keras.io> (2015).
- [50] M. Abadi, A. Agarwal, P. Barham, E. Brevdo, Z. Chen, C. Citro, G. S. Corrado, A. Davis, J. Dean, M. Devin, S. Ghemawat, I. Goodfellow, A. Harp, G. Irving, M. Isard, Y. Jia, R. Jozefowicz, L. Kaiser, M. Kudlur, J. Levenberg, D. Mané, R. Monga, S. Moore, D. Murray, C. Olah, M. Schuster, J. Shlens, B. Steiner, I. Sutskever, K. Talwar, P. Tucker, V. Vanhoucke, V. Vasudevan, F. Viégas, O. Vinyals, P. Warden, M. Wattenberg, M. Wicke, Y. Yu, and X. Zheng, “TensorFlow: Large-scale machine learning on heterogeneous systems,” (2015).